

## Article

# Deformation Mechanism and Structural Changes in the Globular Ti-6Al-4V Alloy under Quasi-Static and Dynamic Compression: To the Question of the Controlling Phase in the Deformation of $\alpha+\beta$ Titanium Alloys

Pavlo E. Markovsky <sup>1</sup>, Jacek Janiszewski <sup>2</sup> , Olexander Dekhtyar <sup>1</sup>, Matthew Mecklenburg <sup>3</sup>  
and Sergey V. Prikhodko <sup>4,\*</sup>

<sup>1</sup> G.V. Kurdyumov Institute for Metal Physics of NAS of Ukraine, 36, Vernadsky Blvd., 03142 Kyiv, Ukraine; p\_markovsky@yahoo.com (P.E.M.); dekhtyar@imp.kiev.ua (O.D.)

<sup>2</sup> Faculty of Mechatronics and Aviation, Jarosław Dąbrowski Military University of Technology, 2, gen. Sylwester Kaliski Str., 00-908 Warsaw, Poland; jacek.janiszewski@wat.edu.pl

<sup>3</sup> Core Center of Excellence in Nano Imaging (CNI), University of Southern California, Los Angeles, CA 90089, USA; m.h.mecklenburg@gmail.com

<sup>4</sup> Department of Materials Science and Engineering, University of California, Los Angeles, CA 90095, USA

\* Correspondence: sergey@seas.ucla.edu; Tel.: +1-310-825-9735



**Citation:** Markovsky, P.E.; Janiszewski, J.; Dekhtyar, O.; Mecklenburg, M.; Prikhodko, S.V. Deformation Mechanism and Structural Changes in the Globular Ti-6Al-4V Alloy under Quasi-Static and Dynamic Compression: To the Question of the Controlling Phase in the Deformation of  $\alpha+\beta$  Titanium Alloys. *Crystals* **2022**, *12*, 645. <https://doi.org/10.3390/cryst12050645>

Academic Editors: Maria Cecilia Poletti, Silvana Sommadossi and Ricardo H. Buzolin

Received: 31 March 2022

Accepted: 27 April 2022

Published: 1 May 2022

**Publisher's Note:** MDPI stays neutral with regard to jurisdictional claims in published maps and institutional affiliations.



**Copyright:** © 2022 by the authors. Licensee MDPI, Basel, Switzerland. This article is an open access article distributed under the terms and conditions of the Creative Commons Attribution (CC BY) license (<https://creativecommons.org/licenses/by/4.0/>).

**Abstract:** The deformation mechanism of the Ti-6Al-4V (wt.%) alloy with globular structure was studied under conditions of quasi-static and high-strain compression with rates  $10^{-3} \text{ s}^{-1}$  and  $2.1\text{--}3.3 \times 10^3 \text{ s}^{-1}$ , respectively. High-strain compression was conducted using a Split Hopkinson Pressure Bar (SHPB). The details of the deformation mechanism were evaluated based on the analysis of the deformation hardening curves using the *strain hardening exponent* concept developed for titanium alloys in tension conditions. The used approach allowed us to identify the stages of plastic deformation observed and the controlling phase in deformation of two-phase alloy through the assessment of the strengthening index, *n*. It has been found that three deformation stages can be identified in quasi-static conditions. However, when the alloy is compressed at a high strain rate, the third deformation stage does not develop due to the high process rate. Further analysis of deformation curves reveals the leading role of the  $\beta$ -phase under the quasi-static conditions and the essential contribution of the second,  $\alpha$ -phase, at a high compression rate. The findings on the deformation mechanism based on the analysis of hardening curves were supported by a detailed structural study.

**Keywords:** titanium alloy; quasi-static compression; high-strain compression; Split Hopkinson Pressure Bar; plastic deformation; strain hardening exponent

## 1. Introduction

A number of studies of titanium alloys are devoted to the influence of external load on the deformation mechanism and microstructure of alloys, since such studies explain the physical and mechanical, and, ultimately, operational properties of these materials [1–7]. The main attention in these works is paid to the details of imposed temperature-loading conditions of deformation treatment on the mechanism and the characteristics of deformation hardening and/or softening due to possible recovery or recrystallization and it is clear that the deformation mechanisms and the depth of the deformation processes taking place in the same structure are strongly dependent on the conditions the load was applied. In this regard it is considered that four different stages of plastic deformation might be specified: when the first stage is characterized by multiple generations of dislocations; the second with the formation of the dislocation networks and clusters; the third stage is specified by the formation of the cell structure; and finally, the fourth stage is designated by the

dynamic recovery. Not all of these stages are necessarily present in all testing conditions. The depth of the structural changes that occur due to the plastic deformation depends on the temperature-loading conditions and the presence of a specific stage can be adequately confirmed by the study of the final structure, so generally, the acting mechanisms and their completion can be rendered. Additional complexity to all these varieties of possible intricate mechanisms, their completion, and the combination is added due to the phase conditions of the alloy and if there is more than one phase involved, like it is in some titanium alloys, that can give a different outcome in  $\alpha$ - [1],  $\alpha+\beta$ - [1–4], and  $\beta$ - alloys [1,5–8] since the deformation behavior of each phase is substantially dissimilar. The question of what phase plays the leading role in the deformation process of the two-phase alloy is not a simple matter of presumably acting rule of mixtures, since two phases have different abilities to deform plastically and this ability also depends on the imposed temperature-loading conditions, structure strengthening component, structure morphology, orientation, strain partitioning effect, etc. [6]. It is believed that the structural component plays one of the leading roles in the strengthening of Ti alloys [2–5]. Each phase strengthens differently and their contribution to the final strength of the alloy will not be the same. A phase that deforms at a higher stress level *plays a leading role in deformation*. That is why the important question is to determine the leading phase, which controls the deformation process of the entire alloy. Significant attention has also been and continues to be paid to the study of deformation processes at ambient temperatures of such alloys [9–11], since an understanding of deformation mechanisms under such conditions can suggest the parameters of operation and predict the reliability of real products made from these alloys. Among these studies, it should be separately noted some works [12–14], in which a relationship was established between the mechanical behavior at various stages of deformation described by stress-strain curves and the evolution of microstructure studied at various stages of deformation. This relationship was most successfully shown for studies of quasi-static tension at room temperature, as confirmed for a wide range of metals and alloys with different crystalline structures. This approach made it possible to define deformation mechanisms for different stages of development of the homogeneous plastic flow of these materials. For example, V.F. Moiseev and colleagues showed that the homogeneous stage of the plastic flow of metals under tension can be expressed in terms of true stress  $\sigma$  vs. true strain  $\varepsilon$  [12,13], and the phase composition and structural state of these alloys play a pivotal role in qualitative analyses of the deformation outcome. The authors used the *strain hardening exponent* concept when the stress-strain curve of the uniform stage of plastic deformation (before its localization and the neck appearance) can be expressed as:

$$\sigma = \sigma_{0.2} + B_s \varepsilon^n, \quad (1)$$

where  $\sigma_{0.2}$ —is stress at a 0.2% strain,  $B_s$ —is a strengthening coefficient, and  $n$ —is a strengthening index. Then the stage of uniform deformation processed in  $\sigma - \varepsilon^n$  coordinates implies the detection of inflections on hardening curves corresponding to the change of structural states characterized by specific values of  $n$ . As a result of numerous experiments involving interruption of the tension test at different stages followed by a detailed examination of the microstructure of the samples, it was found that each stage is associated with a certain type of dislocation structure that corresponds to a specific strengthening coefficient,  $n$ . Typically, a uniform stage of plastic metal flow in the annealed state with a low initial defect density is divided into three rectilinear portions, the described above stages of the plastic deformation process, when the 4th stage is not always specifically registered due to the experimental set up (which usually require prolong testing times). In addition, by comparative analysis of the tensile curves of metals with different crystal structures, it was found that each type of crystal lattice predetermines a specific value of the hardening index,  $n$  [12,13]. For example, the Hexagonal Close-Packed (HCP) lattice is characterized by the hardening index  $n = 0.8-1$ , while the Body Centered Cubic (BCC) lattice is characterized by  $n$  close to 0.5. With the development of these works, it turned out that this approach is also applicable to two-phase titanium alloys [13–15], where it was possible to establish which phase,  $\alpha$  or  $\beta$

plays a leading role in the process of plastic deformation by directly measuring the value of the coefficient  $n$  from the stress-strain curves established for two-phase material.

Similar studies on compression, in both quasi-static and dynamic conditions, are not reported. An exception are the works on the study of quasi-static compression of the metastable  $\beta$ -phase, which caused, among others, its decomposition with the formation of martensite of deformation [16]. However, in our recent study [17] of the mechanical behavior of the alloy Ti-6Al-4V (weight percent), hereafter referred to as Ti64, the microstructure was investigated in the conditions of quasi-static and dynamic compression. In particular, it was found that under the high-strain rate compression using the Split Hopkinson Pressure Bar (SHPB) test, the alloy with a globular microstructure is superior in strength and ductility over the alloy with a lamellar microstructure. Namely, the samples with a globular microstructure remain unfractured when they were tested at a high-strain rate of up to  $3200 \text{ s}^{-1}$ , while samples with a lamellar structure were already broken at the strain rate of  $1950 \text{ s}^{-1}$ . The corresponding measured values of maximum deformation energy were also substantially different: 2795 J and 1594 J. In order to explain the physical nature of observed superiority of the globular microstructure, a hypothesis was put forward about the critical role of the microstructure (morphology of the  $\alpha$ -phase) and the type of interfacial boundaries involved in the transmission of plastic deformation between crystals. It was suggested that  $\alpha/\alpha$  boundaries predefine the properties in the globular structure of this alloy, while  $\alpha/\beta$  interphase boundaries in the lamellar. Such interactions warrant further research to develop a holistic understanding of the underlying physical mechanisms which are operative on the critical scales.

With the above in mind, the purpose of the present study was a further exploration of the mechanical properties and structure of the Ti64 alloy with globular microstructure based on the analysis of the deformation hardening curves of this alloy using the *strain hardening exponent* (SHE) concept for quasi-static and high-strain rate compressions; determining the role of each phase in the study conditions and the possibility of changing this role depending on the test conditions.

## 2. Materials and Methods

The alloy Ti64 was purchased in a shape of 10 mm diameter rods from Perryman Company (Houston, PA, USA). The material was annealed at  $850 \text{ }^\circ\text{C}$  for 2 h and then cooled with a furnace, which resulted in the formation of a uniform microstructure of globular type. Cylindrical specimens with the same geometry, diameter, and height of 5 mm, were machined and used for compression tests in both modes: quasi-static and dynamic. The last one, high-strain rate compression, was performed with the use of the SHPB, also called a Kolsky bar technique [18,19]. More details on the used experimental set up were recently reported elsewhere [17,20], including a detailed description of the procedure for determining all parameters in these high strain rate tests [17]. Materials were studied using a scanning electron microscope (SEM), Vega 3 (Tescan, Czech Republic). Crystal orientation and phase mapping were performed using Electron Back Scatter Diffraction (EBSD) on bulk samples and Transmission Kikuchi Diffraction (TKD) on electron transparent samples. EBSD and TKD measurements were made using the Symmetry EBSD Detector (Oxford Instruments, Abingdon, Oxfordshire, UK) installed on a Helios G4 UXe PFIB (Thermo Fisher Scientific, USA), which was equipped with UltimMax 170 Silicon Drift Detector (Oxford Instruments, Abingdon, Oxfordshire, UK) for measuring elemental composition of materials by energy dispersive spectroscopy (EDS). Electron transparent samples were prepared from specific locations on the bulk samples using the lift-out method on a Nova NanoLab 600 DualBeam (Thermo Fisher Scientific, Waltham, MA, USA). Transmission electron microscopy TEM was performed using STEM Titan 80-300 TEM (Thermo Fisher Scientific, Waltham, MA, USA).

### 3. Results and Discussion

It is well-known that under uniaxial compression in quasi-static conditions, the bulk cylinder sample undergoes uniform compression along the axis of applied load and uniform tension in a direction perpendicular to that axis. The situation can be different in dynamic conditions when compression is applied at high rates. In this case, the deformation can be uneven within the entire bulk sample. Previously, a scheme based on Schmitt's law has been proposed for identifying various deformation zones that occur at the macro-level in a cylinder sample during compression under conditions where a load is applied at a high rate [17]. This scheme is reproduced herein in Figure 1a. This implies the existence of four different deformation zones, which are formed in the sample under compression at a high strain rate and thus can create different microstructures. According to this scheme and depending on the applied strain rate, different areas of plastic flow were predicted, where deformation is differently localized at the macro-level in zones A, B, C, and D; plastic deformation is uniform inside each zone, but different outside each. It is important to note that most of the sample is represented by zone D, so it can be argued that the bulk of the sample still deforms uniformly except for a smaller number of its portions. The validity of such a scheme has recently been confirmed in high-strain rate compression experiments by directly observed structural changes after the test, which confirm the presence of plastically different deformed zones within the cylindrical sample [17]. The observed structural changes and experimentally measured strain hardening curves in this study are analyzed here in light of this scheme.

The images in Figure 1c,d show the structure of the samples after the quasi-static compression test and this structure was uniform thorough the bulk of the cylinder sample. The images in Figure 1e–g show microstructures that are formed in the deformation zone D when the test samples are subjected to high-strain compression at different rates. Zone D was a large part of the cylinder, and zones A–C were a small part of it. The details of the structure in the various zones are communicated elsewhere [17], here we are trying to establish a deformation mechanism for most of the bulk sample, namely zone D. There is a striking difference between the morphology of the structure observed within the bulk of the sample after its compression in quasi-static mode and testing with a high-strain rate. The globular structure typical of the pre-test alloy shown in Figure 1b has become uniformly plastically deformed (c, *ibid.*), apparently elongated perpendicular to the applied load (vertical in the image). While the structure compressed at high rates shown in Figure 1e does not seem to be so different compared to the original structure: grains seem to retain their globular morphology, although numerous twins appear inside the globules. The observed structural changes suggest that different mechanisms of plastic deformation operate under different test conditions, namely at different strain rates.

The original curves of true stress vs. true strain of materials tested under compression at different rates are presented in Figure 2a. A detailed discussion of these curves was given in the previous work [17]. Here, it can be summarized that as the strain rate increases, the strength of the samples increases for all tested samples, as shown by curves 1–5 in Figure 2a. In the high-strain rate tests shown in curves 2–5, when the strain rate increased, both the strength of the samples and the ductility of all samples increased, and even at a maximum deformation rate of  $3320 \text{ s}^{-1}$ , the alloy sample did not fracture probably due to increased plasticity. The original experimental data for different strain rates, labeled 1–5 in Figure 2a were further processed using the regression analysis. The results of such analysis are shown for each strain rate in a separate diagram presented in Figure 2b–f with the detailed data analysis steps taken for the quasi-static compression case shown in Figure 2b and only the final analysis result (to prevent the difficulty of the diagrams reading) for the remaining data (c–f, *ibid.*). The result of the regression analysis giving the number of deformation stages and hardening index  $n$  were selected manually for each strain rate to ensure the best fit to the experimental data. All experimental raw curves 1–5 were individually fitted with the exponential function according to Formula (1), with the exponent varied from 1 to 0.5, which are the possible values of the strengthening index

$n$ , and the used increment was 0.1. This analysis made it possible to find the best fit to the exponential function of the experimental curve, in which linear sections can be further applied to match the experimental data. As a result, two important factors were found from the best fit for each strain rate, namely the index  $n$ , which defines the controlling phase of the deformation process, and the number of linear sections, which determines the possible number of deformation stages.

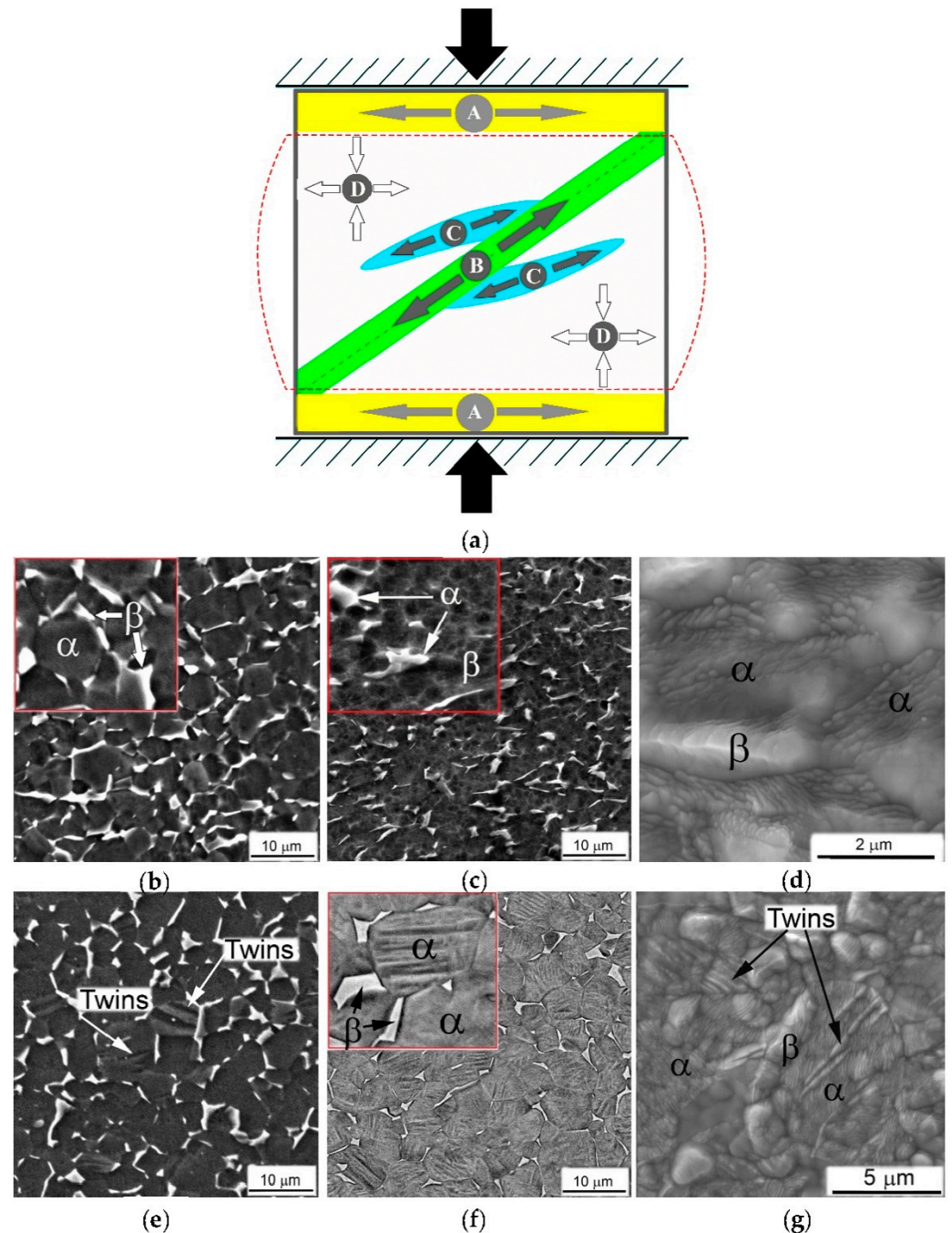


**Figure 1.** Schematic representation of specific zones where deformation is differently localized at *macro-level* shown in the longitudinal section of tested cylindrical specimen (a)—A–D denote a specific zone; the arrows indicate the direction of the acting forces [17]; observed microstructure of Ti64 alloy in (b) initial state, and after (c,d) quasi static (strain rate  $10^{-3} \text{ s}^{-1}$ ), and (e–g) SHPB compression with strain rates (e)  $2100 \text{ s}^{-1}$ , (f)  $2500 \text{ s}^{-1}$ , and  $3320 \text{ s}^{-1}$  (g). SEM: (b–e,g) SE, (f) BSE.

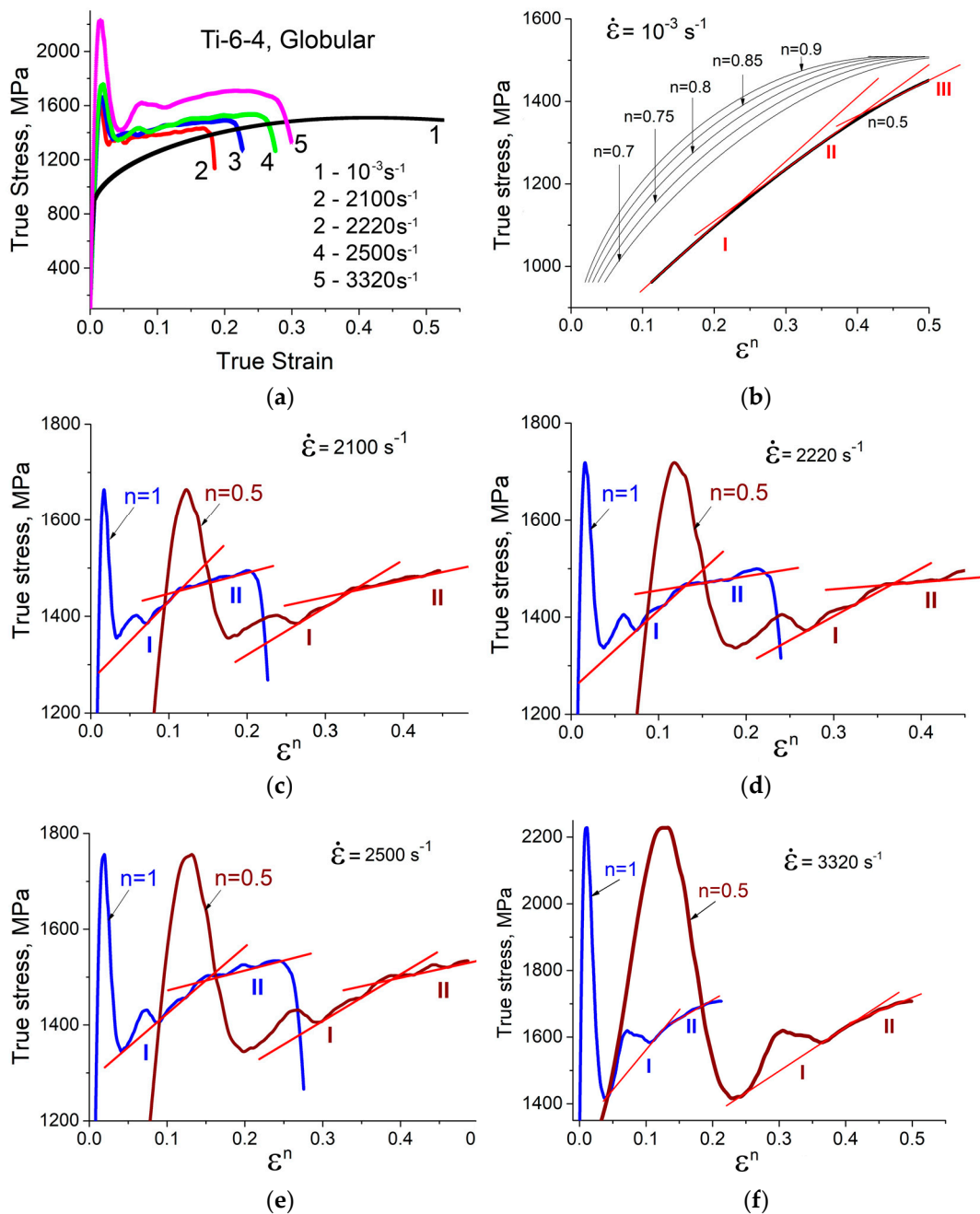


**Figure 2.** True stress-true strain curves for Ti64GL specimen compression tested with the different strain rates (a); Analysis of stress-strain curves for: (b)—quasi-static compression with rate  $10^{-3} \text{ s}^{-1}$ , and high strain rate SHPB tests with rates (c)— $2100 \text{ s}^{-1}$ , (d)— $2220 \text{ s}^{-1}$ , (e)— $2500 \text{ s}^{-1}$ , and (f)— $3320 \text{ s}^{-1}$ .

Results of regression analysis for the quasi-static test with the strain rate  $10^{-3} \text{ s}^{-1}$  are presented in Figure 2b. They show that the best fit of the experimental data with exponential function is observed for the strengthening index  $n$  of 0.5, and the presence of two inflections on hardening curves at  $\epsilon^n$  close to 0.25 and 0.4 imply three linear sections to fit the experimentally measured true stress data. Following the SHE concepts, the first important statement can be made regarding the controlling role of  $\beta$ -phase in the deformation process of this alloy under conditions of quasi-static compression, since the determined strengthening index  $n = 0.5$  is the value characteristic of BCC metals. This suggests that the  $\beta$ -phase deforms at a higher stress level. Despite the fact that the volume fraction of  $\beta$ -phase in this alloy is not significant (around 7% in our case), it controls the

deformation under compression, and the strengthening of the alloy is a typical mechanism for composites. The earlier published study [14] on the deformation mechanism of the same alloy Ti64 but tested under tension reports a different strengthening index giving its value of  $n = 0.81$ , which suggests the leading role of  $\alpha$ -phase in tension. Thus, it can be seen that in quasi-static conditions the strain partitioning effect for this alloy is quite different depending on the type of the load. In fairness, it should be noted that unfortunately the used strain rate in the above-mentioned study is not reported, but based on the context of the published data the rate was most likely close to the quasi-static conditions used in the current study. The second important statement can be made in accordance with the used SHE concept, this is the existence of three deformation stages under tested conditions, since there are two bends on the hardening curve, which imply three linear sections to fit the experimental data.

The next step in the used approach will be to assess the experimentally observed structure in terms of its compliance with stated assumptions. A comparison of the SEM images of the initial structure (Figure 1b) and the structure formed during quasi-static compression (Figure 1c,d) does not contradict the leading role of the  $\beta$ -phase in the mechanism of strain hardening of the Ti64 alloy with a globular structure. The  $\beta$ -phase layers play the role of “coating”  $\alpha$ -globules and “links” transmitting the deformation between  $\alpha$ -globules starting from the initial state (Figure 1a) and throughout compression (Figure 1c,d). During the ongoing deformation, the  $\alpha$ -phase is deformed more and more, forming not only a high dislocation density inside the globules, but also dislocation networks and clusters, and ultimately the cell structure is formed (Figure 1d). Frankly, the presented images demonstrate only the end result of such an evolution of the structure, its  $\alpha$ -globules cell morphology, but it is obvious that the observed final result of such evolution can only develop through all three stages discussed above. The outcome of the structural assessment is fully in compliance with the results of the regression analysis presented in Figure 2b. The presence of two bends on the hardening curves at  $n = 0.5$  fit gives three linear sections, assuming the presence of the three deformation stages. The initial stage indicated by line I in Figure 2b corresponds to the multiple dislocations’ generation and their free motion. The second stage, indicated by II, basically corresponds to the accumulation of dislocations and the formation of their coils. And the third stage, indicated by III, relates to the cellular substructure formation with non-oriented cell boundaries in the  $\alpha$ -phase (Figure 1c).

The deformation mechanism of the alloy Ti64 appears to be quite different when compression is applied at high strain rates. First of all, it is reflected by the set of true stress vs. true strains curves shown in Figure 2c–f, which demonstrate a similar character for the strain rates  $2.1\text{--}3.3 \times 10^3 \text{ s}^{-1}$ , but very different when compared to the discussed above quasi-static compression test. All SHPB stress-strain curves show the initial stress peak, which nature is a rather complex interaction of various factors and was described in detail in a number of works [19,21–23]. The essence of the problem comes down mainly to technical features of the testing method, namely, the inertia of the ongoing processes of load transfer and deformation propagation, inhomogeneity of deformation along the length and cross-section of the sample, the effect of the ratio between the dimensions of the installation’s bars and the sample, etc. Here we simply ignore this peak in the used regression analysis and account only for the regions of uniform plastic deformation following these peaks.

When analyzing curves recalculated in true stress— $\epsilon^n$  coordinates, straight tangent lines were drawn along the minima, which correspond to the stress relaxation points during deformation. It is evident that after recalculation, all curves for strain rates 2.1, 2.22, 2.5, and  $3.32 \times 10^3 \text{ s}^{-1}$  are quite similar. The first important conclusion that can be made is that regardless of the used strengthening index  $n$ , which was varied in the range from 0.5 to 1.0, the observed experimental results are well fit with using two straight sections, that correspond to two deformation stages indicated by lines I and II in Figure 2c–f. The fit was generally the same for all used values of  $n$ , suggesting that there is no leading phase controlling the deformation process, and both phases, BCC and HCP, contribute equally.

This result is quite different from what was observed under quasi-static compression discussed here above when only one value of the strengthening index  $n = 0.5$  was obviously giving the best fit, suggesting the BCC phase plays a leading role in deformation. This result is also different from the one previously published on the quasi-static tension [12–14,24,25] when the found strengthening index was also a single value  $n = 0.81$  suggesting the leading role of the HCP phase. Despite the differences in the leading phase in both quasi-static compression and tension all strengthening mechanisms are associated with dislocations, i.e., with shear deformation [26]. In both cases of quasi-static testing there is a gradual change in the dislocation system observed from single dislocations to their networks and clusters and finally, the developed cell structure, which is reflected well in three stages of deformation. Consequently, the strengthening mechanism is described, by a single hardening index  $n$  associated with a certain phase that controls this hardening process. The observed fact that in dynamic compression curves can be described by using different values of  $n$  differs drastically from the quasi-static conditions, which suggests at least another deformation mechanism in action. The structure of the alloy tested in dynamic conditions shows numerous twins (Figure 1d–g) indicative of active deformation with rotation mode [27,28]. It is evident that besides the acting twinning mechanism the deformation is also observed by the shear. This is supported by the presence of two straight sections in all considered cases of fitted experimental data in Figure 2c–f. Obviously in the last, second stage of deformation, the observed hardening is associated with the formation of a dispersed cellular substructure, which is visible in both the  $\alpha$ - and  $\beta$ -phases (Figure 1f). Most likely, in compression with a high strain rate, the first deformation stage is associated with the formation of a high-density dislocation network [29], which in the second stage are transformed into dislocation cells, and in the final structure coexist with twins (Figure 1g).

The above analysis of deformation curves and the corresponding structures suggests that during dynamic compression of the Ti64 alloy with the globular structure, both phases, the  $\alpha$  and  $\beta$ , simultaneously control the work hardening, as evidenced by the values of the hardening index  $n$  varying from 0.5 to 1. In this case, the deformation is provided simultaneously by both mechanisms involving the work of dislocations and twins. The possibility for the alloy to deform by twinning also explains the observed improved ductility of the alloy under the high strain rates as shown by curves 2–5 in Figure 2. When the strain rate increased, both the strength of the samples and the ductility of all samples increased, and even at a maximum deformation rate of  $3320 \text{ s}^{-1}$ , the alloy sample did not fracture apparently due to increased plasticity.

The SEM images presented and discussed here before provide a general understanding of the deformation process and structural changes involved. For instance, under conditions of quasi-static compression, when the deforming external force is applied relatively slowly giving enough time for the steady plastic flow and the processes of stress relaxation, a developed cellular substructure is finally formed in the  $\alpha$ -phase (Figure 1d). Such structural change well agrees with the conclusions drawn from the analysis of the curves in Figure 2b that gives three stages of the deformation process. In the case of high-strain rate compression, the defectiveness of the  $\beta$ -phase looks much more pronounced and the regions of this phase became even separated into cells or subgrains, and even individual fragments, while the globules of the  $\alpha$ -phase look strongly deformed close to the boundary regions (Figure 1g). Therefore, for a better understanding of specific details of plastic deformation under high-rate load, additional studies of crystallinity of deformed samples were carried out using the conventional EBSD performed on the tested sample within the zone D (Figure 1a) and TKD EBSD performed on the sample cut using focused ion beam (FIB) from the specific area located on the A and D interface zone (ibid). Choosing the region on the interface of zone A and D actually allowed us to evaluate the structure development beyond the changes predicted by the strengthening curves analysis following the SHE concepts, since zone A represents the area of adiabatic shear bend (ASB). The same sample prepared via FIB and initially used for TKD analysis was also suitable for the following conventional TEM, which greatly complimented TKD data.

Figure 3 shows the results of conventional EBSD taken in the bulk sample at zone D (Figure 1a). As can be seen from the pattern quality map (PQM) in Figure 3a the deformation defects are distributed very heterogeneously over different  $\alpha$ -globules. For example, three neighboring globules labeled in the figure as K, L, and M have essentially different densities of defects. The density increases from almost defects-free crystal K to crystal L, and finally to crystal M. Globule K does not show much contrast variation in the PQM image. The corresponding inverse polar figure (IPF) image in Figure 3f depicts this crystal in the same color (purple), which is indicative of no significant change in orientation within the entire globule. Globule L contains more defects and shows that some of its areas are misoriented at about 30 degrees within about 7  $\mu\text{m}$  range. The globule L color in the IPF map is gradually changing from green to dark blue, indicating the beginning of the walls' formation in this crystal. The globule M already shows a relatively small subgrain. The globule M color in the IPF image is changing abruptly and two different parts of the grain are misoriented at about 20 degrees within a 5  $\mu\text{m}$  range (Figure 3f). The grain misorientation map (GMM) in Figure 3c indicates that the peripheral parts of each  $\alpha$ -globule (shown in green) are misoriented relative to their centers (shown in blue) by about 2–2.5 degrees. Such misorientation is sufficiently uniform throughout the structure, suggesting that the boundaries between crystals  $\alpha/\alpha$  and  $\alpha/\beta$  play an important role in the deformation process. As for  $\beta$ -phase crystals, they cannot be easily detected with conventional EBSD, since they are usually represented by layers between the  $\alpha$ -crystals and rarely have a thickness of several micrometers, but in most cases, they have a thickness from submicrometers to several tens of nanometers, which are at the level of detectability with conventional EBSD [30]. The plastic deformation of  $\beta$ -phase crystals and the absence of perfect crystallinity also added to the complexity of their detection. However, some relatively bigger  $\beta$ -crystals are seen in the phase map (Figure 3d) and the EDS elemental map of vanadium (Figure 3b) clearly shows the expected fraction of the  $\beta$ -phase for this alloy (about 10%). In addition, it is important to mention that some larger  $\alpha$ -globules are surrounded by black regions seen in the PQM (Figure 3a), phase map (d), and the GMM (e), which often represent strongly deformed regions that cannot give high quality Kikuchi lines, but also can result from dimensional limitation factor, which exists for the  $\beta$ -phase detection. It can also be noted that according to the IPF orientation map image (Figure 3d), the majority of  $\alpha$ -phase bigger crystals demonstrate relatively high mutual misorientation (15–20 degrees) and some twins can also be seen in the image; for example, a twin in  $\alpha$ -grain marked N in the PQM and visible on the IPF of Figure 3.

Summarizing the results of conventional EBSD shown in Figure 3, it can be concluded that under the high strain-rate compression, uniform (on the macro-level) stage of plastic deformation is mostly localized in the peripheral regions of  $\alpha$ -globules near their boundaries, which implies highly nonuniform plastic deformation on the micro-level. As a result, a deformed shell is formed along the interfaces of the  $\alpha$ -particles, leaving the main part of the globules substantially free from defects.

A detailed study of the fine structure was additionally performed using a lift off sample prepared by FIB and TKD analyzed in SEM followed by conventional TEM. The sample cut-off area was selected at the boundary between the highly deformed sample area represented by zone B (Figure 1a) where the adiabatic shear band (ASB) was formed during the compression test and zone D (ibid) representing the majority of the bulk sample discussed above. For this purpose, SEM was used in backscattered electron imaging mode, which allows for a clear identification of structures and phases (Figure 4a). The selected area is marked with a red section in Figure 4 and it simultaneously captures different structures, namely—(1) ASB, (2)  $\alpha$ -phase globule, and (3)  $\beta$ -phase layer (Figure 4a,b).

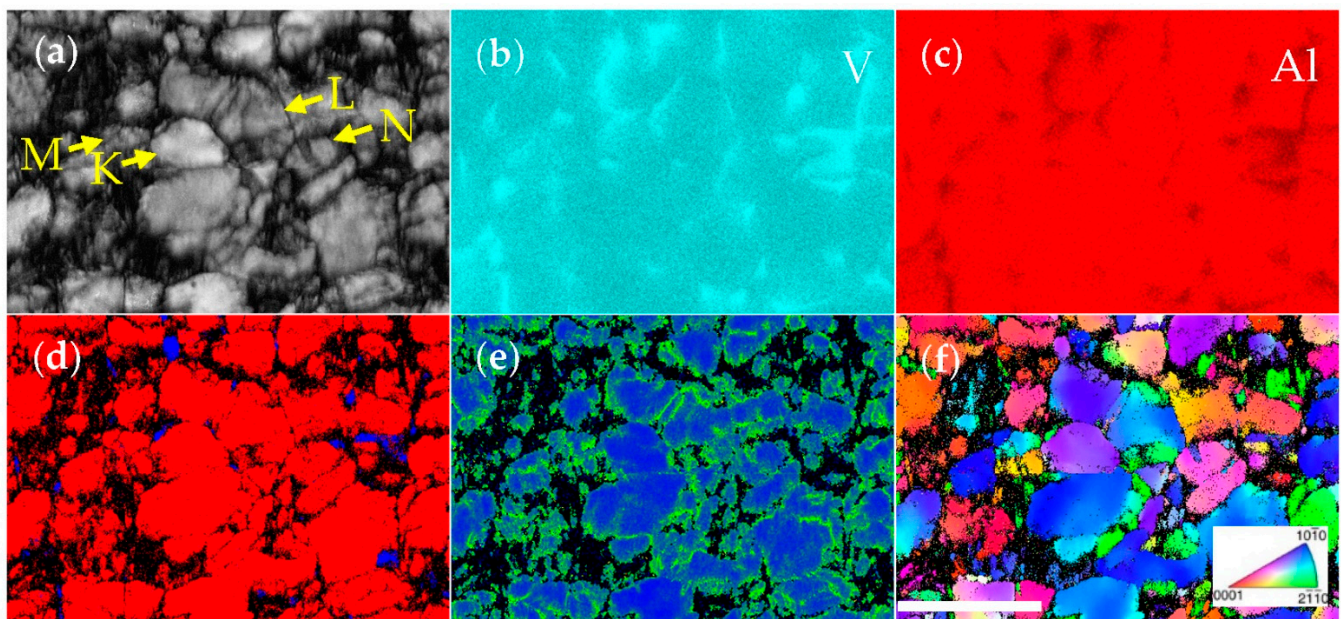


**Figure 3.** SEM images of the Ti64GL sample after its SHPB test (strain rate  $2200 \text{ s}^{-1}$ ) within conventional EBSD and EDS analyses. The presented area was located inside the zone D (Figure 1a). The Pattern Quality Map (PQM) (a); elemental maps V and Al (b,c) correspondingly; phase map image (d), where  $\alpha$ -phase is shown in red,  $\beta$ -phase in blue; Grain Misorientation Map (GMM) (e), the green areas are misoriented from blue on about 2–2.5 degrees; orientation map image (IPF) (f). The scale bar in (f) is  $10 \mu\text{m}$ .

The TKD results of the compressed sample zone D shown here are in compliance with conventional EBSD data presented in Figure 3. A closer view of  $\alpha$ -globule, possible with TKD confirms that most defects are formed near the grain boundaries, while the central portions of the grain have significantly fewer defects. Some parts of the globule closer to the boundaries, show relatively greater misorientation toward the globule center. The  $\alpha$ -globules closest to the ASB demonstrate significant misorientation and some fragmentation. Finally, the ASB region is represented by highly fragmented and recrystallized areas, which alternate strongly deformed regions of the same globule. As for the  $\beta$ -phase layers, similar features of their defective structure can be observed, but in fairness, it must be said that they are not so obvious due to the dimensional factor already discussed above.

The TEM study of the same sample largely compliments the TKD results done in the SEM. These are presented in Figure 5. It can be seen that the central portions of the  $\alpha$ -globules are not very dense with defects even within 1–3 microns away from the highly deformed region of the sample, which is regarded as the ASB region. The corresponding diffraction pattern of region A in Figure 5c shows that the selected area is a single crystal close to the  $[01\bar{1}2]$   $\alpha$  zone with its two parts slightly misoriented (about 5 degrees), since most of the diffraction spots are doubled. Besides, the observed conventional broadening and blurring of the spots are common to Ti alloy with non-highly defected structures. The region B diffraction pattern is taken at the  $\alpha/\beta$  interphase boundary at about the same distance from the ASB as the region A diffraction was taken. It demonstrates a significantly higher density of defects in this region. The elongation of some spots in the azimuthal direction is about  $15+$  deg., which is indicative of significant misorientation of some parts of  $\alpha$ - and  $\beta$ -crystals within the 0.5-micron range. It correlates well with TKD/SEM results indicating strong plastic deformation of the structure in the vicinity of  $\alpha/\beta$  boundaries. Finally, diffraction from the most plastically deformed region C corresponding to the ASB structure is indicative of a completely recrystallized structure. This result agrees well with recently published data [31] on ASB structure studied in Ti64 based composites. Few words can be said about the formation mechanism of the ASB based on the images in

Figures 4a and 5a. The flow of material is apparent near the ASB, making some of the  $\alpha$ -globules highly elongated along the stretch resembling a “sugar candy making” mechanism. The direction of such flow is predicted by the macro-level deformation model shown in Figure 1a. Presented here experimental data verify high localization and nonuniformity of structure elongation and it is unmistakable in the TEM image within the  $\alpha+\beta$  labeled region (shown by the dashed arrows in Figure 5a). Evidently, the mechanism of forming the ASB structure includes the step of  $\alpha$ -grains elongation with forming the texture and then the fragmentation of the stretched grains perpendicular to the elongation direction.

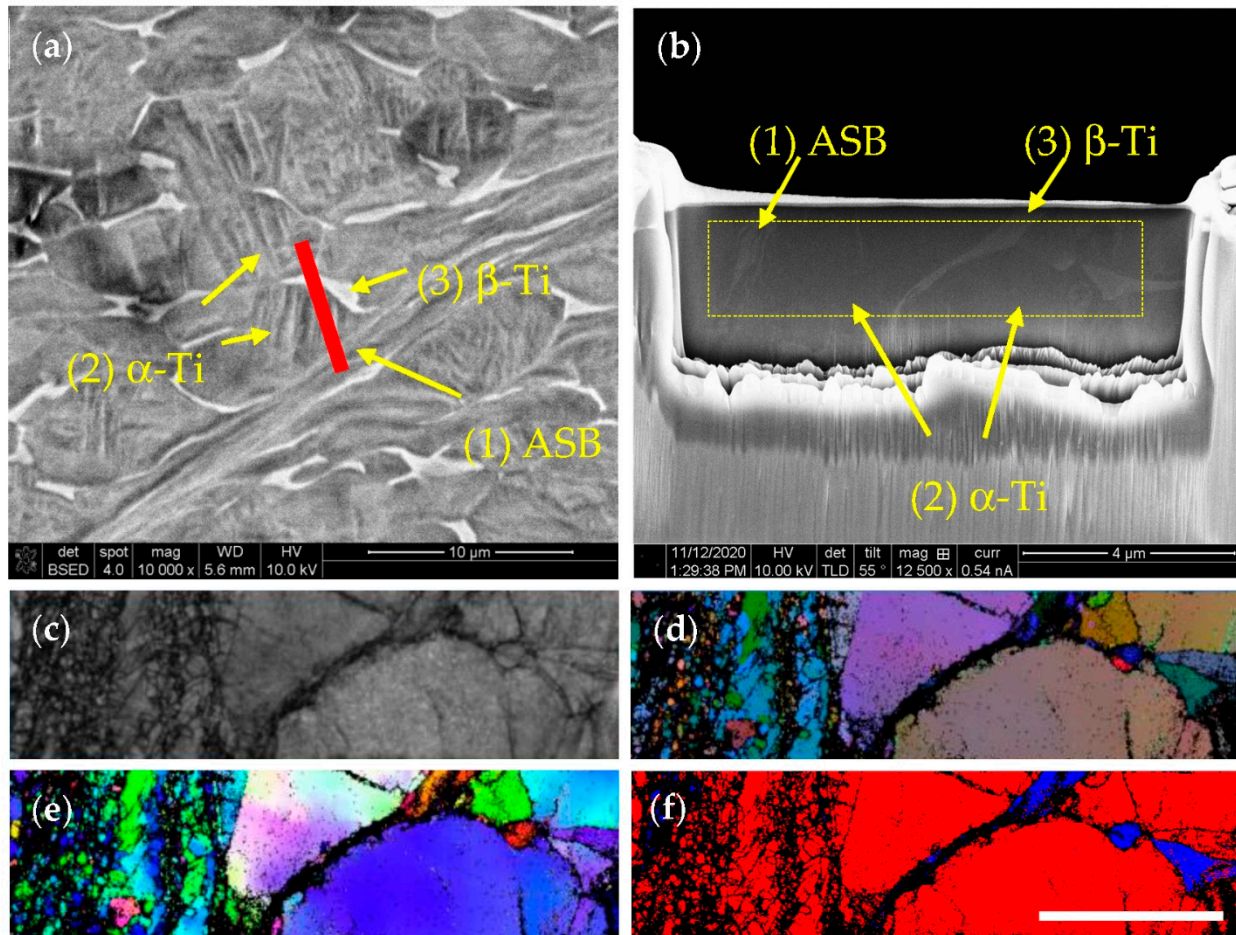


**Figure 4.** SEM images (a,b) of the area in vicinity of ASB (border between zone B and D (Figure 1a) where the lift-off sample was cut and (c–f) TKD framework data. The sample cut (shown with red section) crosses important structural components: a few  $\alpha$ - and  $\beta$ -Ti grains (readily distinguished using the backscattered electrons contrast) and the ASB area labeled in (a,b). The image of the sample showing all structural elements within the lift-off region (b) and the TKD analyzed area highlighted with yellow-dashed rectangular. PQM (c); grains map in random color (d); IPF map e; phase map showing  $\alpha$ -Ti in red and  $\beta$ -Ti in blue (f). The scale bar in (f) is 2.5  $\mu\text{m}$ .

As can be seen from the results presented, the strain hardening of the Ti64 alloy with a globular structure under quasi-static compression (with a low strain rate) at a homogeneous stage is controlled by the  $\beta$ -phase, despite its relatively small amount. In the transition to dynamic compression, when the strain rate increases by a factor of  $10^6$ , analysis of the hardening curves shows that the deformation process is controlled by both  $\beta$ - and  $\alpha$ -phases. At the micro level at the  $\alpha/\beta$  interface, this manifests that the  $\beta$ -phase layers, whose thickness does not exceed 500 nm of the  $\alpha$ -globules coating, participate in deformation completely, while for  $\alpha$ -globules, whose size is about 5  $\mu\text{m}$  and more, only boundary regions with a thickness of about 100 nm are highly deformed. At the same time, the

internal parts of these globules do not experience high plastic deformation. This result is reported for the first time: at a high strain rate,  $\alpha$ -phase globules do not have enough time for volumetric deformation and are only deformed close to the interface.

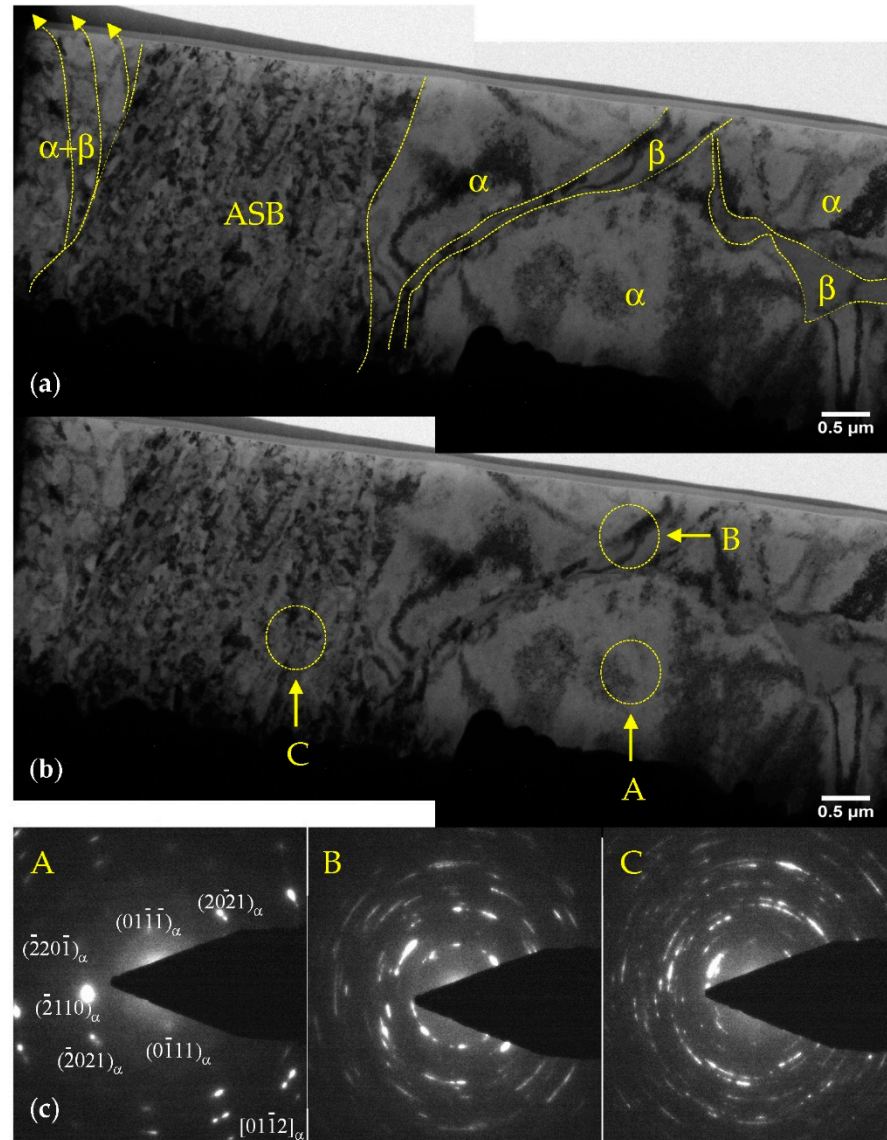


**Figure 5.** TEM results of the lift-off sample studied by TKD/SEM and shown in the Figure 4. Bright-field composite images of entire sample (a,b). The image of the top panel (a) shows different structures captured in the lift-off sample: ASB region, the  $\alpha$ -globules, the  $\beta$ -layers and the fragmented  $\alpha+\beta$  mixture. Dashed lines are used to indicate the boundaries of different structures. The central panel (b) shows the same image as in (a) but with structure boundaries not marked for ease of structure observation. The circled regions A, B and C indicate the location and approximate diameter of selected aperture where corresponding SAED patterns were taken. The bottom panel (c) shows the corresponding SAED patterns of the regions marked in (b).

#### 4. Conclusions

1. Based on the analysis of the deformation hardening curves using the strain hardening exponent concept the details of the deformation mechanism under compression of titanium alloy Ti64 with globular microstructure were evaluated. By assessment, the strengthening index  $n$ , the applied approach revealed the stages of plastic deformation and the phase controlling (deforms at a higher stress level) process of deformation in two-phase Ti alloy.

2. It has been shown that in a quasi-static compression test with a strain rate of  $10^{-3} \text{ s}^{-1}$ , the measured strengthening index  $n$  is 0.5, indicating a controlling role of  $\beta$ -phase. Plastic deformation involves a significant role of dislocation work. Under the quasi-static test conditions, there are three deformation stages with the most advanced stage forming the dislocation cell structure.
3. Under conditions of quasi-static compression, when there is enough time for stress relaxation through the propagation of an external load and movement of dislocations over the bulk of the alloy, the  $\beta$ -phase in the regions of non-localized deformation (like zone D) plays the role of a stress-transferring link. Uniform deformation localization takes place only at the macro-level, according to Schmitt's law.
4. With dynamic compression at rates  $2.1\text{--}3.3 \times 10^3 \text{ s}^{-1}$  both phases, the  $\alpha$  and  $\beta$ , simultaneously control the work hardening, as evidenced by the values of the hardening index  $n$ , varying in the range from 0.5 to 1. In this case, deformation is insured simultaneously by both mechanisms involving the formation of dislocations and twins. The partial ability for the alloy to deform by twinning also explains the observed improved ductility of the alloy under the high strain rates.
5. Under the high strain rate compression there is not enough time for volumetric distribution of the applied external stresses. In this case, the  $\beta$ -phase does not have enough time to transfer the applied load into the volume of most of the  $\alpha$ -phase globules leaving their central volume practically undeformed whereas the majority of the applied external load is transferred to the adjacent  $\beta$ -phase border regions of  $\alpha$ -globules. In other words, during dynamic compression, deformation is localized mainly inside the regions around grain boundaries of the  $\alpha$ -phase globules and in the  $\beta$ -phase interlayers due to the high transience of deformation processes. That is, such form of localization of deformation at the micro-level is a distinctive feature of high strain-rate deformation, in contrast to quasi-static one, when serious localization takes place only at the macro-level, for example, the formation of ASB.
6. Within the zones of macro-localized deformation like ASB and in very thin areas adjacent to them, a whole set of microstructures is formed as a result of localized dynamic deformation. It includes the formation of high dislocation density areas and areas of local overheat caused by deformation making very fine grains appear as a result of recrystallization. However, already at a rather small distance from the ASB, the microstructure is similar to that which is formed in the bulk of the alloy, as in the zone D regions.

**Author Contributions:** Conceptualization, P.E.M., O.D.; methodology, P.E.M., O.D., J.J., S.V.P.; software, P.E.M., J.J.; validation, P.E.M., O.D.; formal analysis, P.E.M., O.D.; investigation, P.E.M., O.D., J.J., M.M., S.V.P.; resources, P.E.M., J.J., S.V.P.; data curation, P.E.M., O.D., J.J., M.M., S.V.P.; writing—original draft preparation, P.E.M.; writing—review and editing, P.E.M., O.D., S.V.P.; visualization, P.E.M., O.D., J.J., M.M., S.V.P.; supervision, P.E.M., S.V.P.; project administration, P.E.M., S.V.P.; funding acquisition, P.E.M., S.V.P. All authors have read and agreed to the published version of the manuscript.

**Funding:** This research was funded by SPS NATO, grant number G5787.

**Institutional Review Board Statement:** Not applicable.

**Informed Consent Statement:** Not applicable.

**Data Availability Statement:** The data presented in this study are available on request from the corresponding author. The data are not publicly available because of the potential for the future invention disclosure.

**Conflicts of Interest:** The authors declare no conflict of interest.

## References

1. Luetjering, G.; Williams, J.C. *Titanium*, 2nd ed.; Springer: Berlin/Heidelberg, Germany, 2007. [[CrossRef](#)]
2. Lütjering, G. Influence of processing on microstructure and mechanical properties of ( $\alpha + \beta$ ) titanium alloys. *Mater. Sci. Eng. A* **1998**, *243*, 32–45. [[CrossRef](#)]

3. Semiatin, S.L.; Seetharaman, V.; Weiss, I. The thermomechanical processing of alpha/beta titanium alloys. *JOM* **1997**, *49*, 33–39. [[CrossRef](#)]
4. Markovsky, P. Preparation and properties of ultrafine (submicron) structure titanium alloys. *Mater. Sci. Eng. A* **1995**, *203*, L1–L4. [[CrossRef](#)]
5. Semiatin, S.L. An Overview of the Thermomechanical Processing of  $\alpha/\beta$  Titanium Alloys: Current Status and Future Research Opportunities. *Met. Mater. Trans. A* **2020**, *51*, 2593–2625. [[CrossRef](#)]
6. Weiss, I.; Semiatin, S. Thermomechanical processing of beta titanium alloys—An overview. *Mater. Sci. Eng. A* **1998**, *243*, 46–65. [[CrossRef](#)]
7. Semiatin, S.L.; Nicolaou, P.D.; Thomas, J.P. Defect Occurrence and Modeling for the Thermomechanical Processing of Aerospace Alloys. *J. Eng. Mater. Technol.* **2008**, *130*, 346–354. [[CrossRef](#)]
8. Ivasishin, O.M.; Markovsky, P.E.; Matviychuk, Y.; Semiatin, S.L. Precipitation and recrystallization behavior of beta titanium alloys during continuous heat treatment. *Met. Mater. Trans. A* **2003**, *34*, 147–158. [[CrossRef](#)]
9. Marteleur, M.; Sun, F.; Gloriant, T.; Vermaut, P.; Jacques, P.J.; Prima, F. On the design of new  $\beta$ -metastable titanium alloys with improved work hardening rate thanks to simultaneous TRIP and TWIP effects. *Scr. Mater.* **2012**, *66*, 749–752. [[CrossRef](#)]
10. Tong, V.; Wielewski, E.; Britton, B. Characterization of slip and twinning in high rate deformed zirconium with electron backscatter diffraction. *arXiv* **2018**, arXiv:1803.00236.
11. Liliensten, L.; Danard, Y.; Brozek, C.; Mantri, S.; Castany, P.; Gloriant, T.; Vermaut, P.; Sun, F.; Banerjee, R.; Prima, F. On the heterogeneous nature of deformation in a strain-transformable beta metastable Ti-V-Cr-Al alloy. *Acta Mater.* **2018**, *162*, 268–276. [[CrossRef](#)]
12. Moiseev, V.F. Effective exponent of deformation strengthening the metals. *Met. Adv. Technol.* **2001**, *23*, 387–399. (In Russian)
13. Kotko, A.V.; Moiseev, V.F.; Pechkovskij, E.P.; Moiseeva, I.V.; Pishchak, V.K. Special features of the plastic deformation of mul-tiphase titanium alloys. *Met. Adv. Technol.* **2001**, *23*, 1013–1027. (In Russian)
14. Moiseev, V.F.; Moiseeva, I.V.; Pishchak, V.K. Influence of  $\alpha$  and  $\beta$ -phases on low- and high-temperature strength of titanium alloy VT6. *Met. Adv. Technol.* **2003**, *25*, 193–203. (In Russian)
15. Dekhtyar, O.I.; Matviichuk, M.V.; Moiseeva, I.V.; Savvakina, D.H. Strain hardening and fracture of VT6 alloy synthesized by the method of powder metallurgy. *Mater. Sci.* **2008**, *44*, 429–434. [[CrossRef](#)]
16. Karasevskaya, O.; Ivasishin, O.; Semiatin, S.; Matviychuk, Y. Deformation behavior of beta-titanium alloys. *Mater. Sci. Eng. A* **2003**, *354*, 121–132. [[CrossRef](#)]
17. Markovsky, P.E.; Janiszewski, J.; Bondarchuk, V.I.; Stasyuk, O.O.; Savvakina, D.G.; Skoryk, M.A.; Cieplak, K.; Dziewit, P.; Prikhodko, S.V. Effect of Strain Rate on Microstructure Evolution and Mechanical Behavior of Titanium-Based Materials. *Metals* **2020**, *10*, 1404. [[CrossRef](#)]
18. Kolsky, H. Propagation of Stress Waves in Linear Viscoelastic Solids. *J. Acoust. Soc. Am.* **1965**, *37*, 1206–1207. [[CrossRef](#)]
19. Kolsky, H. Stress waves in solids. *J. Sound Vib.* **1964**, *1*, 88–110. [[CrossRef](#)]
20. Markovsky, P.E.; Janiszewski, J.; Bondarchuk, V.I.; Stasyuk, O.O.; Cieplak, K.; Karasevska, O.P. Effect of Strain Rate on Mechanical Behavior and Microstructure Evolution of Ti-Based T110 Alloy. *Met. Microstruct. Anal.* **2021**, *10*, 839–861. [[CrossRef](#)]
21. Guo, Y.; Ruan, Q.; Zhu, S.; Wei, Q.; Lu, J.; Hu, B.; Wu, X.; Li, Y. Dynamic failure of titanium: Temperature rise and adiabatic shear band formation. *J. Mech. Phys. Solids* **2019**, *135*, 103811. [[CrossRef](#)]
22. Gray, G.T., III. Classic Split-Hopkinson Pressure Bar Testing. In *Mechanical Testing and Evolution*; ASM Handbook; ASM: Materials Park, OH, USA, 2000; Volume 8. [[CrossRef](#)]
23. Merle, R.; Zhao, H. On the errors associated with the use of large diameter SHPB, correction for radially non-uniform distribution of stress and particle velocity in SHPB testing. *Int. J. Impact Eng.* **2006**, *32*, 1964–1980. [[CrossRef](#)]
24. Markovsky, P.; Matviychuk, Y.; Bondarchuk, V. Influence of grain size and crystallographic texture on mechanical behavior of TIMETAL-LCB in metastable  $\beta$ -condition. *Mater. Sci. Eng. A* **2013**, *559*, 782–789. [[CrossRef](#)]
25. Lee, D.-G.; Lee, S.; Lee, C.S.; Hur, S. Effects of microstructural factors on quasi-static and dynamic deformation behaviors of Ti-6Al-4V alloys with widmanstätten structures. *Met. Mater. Trans. A* **2003**, *34*, 2541–2548. [[CrossRef](#)]
26. Kocks, U.; Mecking, H. Physics and phenomenology of strain hardening: The FCC case. *Prog. Mater. Sci.* **2003**, *48*, 171–273. [[CrossRef](#)]
27. Zhao, G.-H.; Xu, X.; Dye, D.; Rivera-Díaz-Del-Castillo, P.E. Microstructural evolution and strain-hardening in TWIP Ti alloys. *Acta Mater.* **2019**, *183*, 155–164. [[CrossRef](#)]
28. Ostapovets, A.; Serra, A. Review of Non-Classical Features of Deformation Twinning in hcp Metals and Their Description by Disconnection Mechanisms. *Metals* **2020**, *10*, 1134. [[CrossRef](#)]
29. Kotko, V. Strain Hardening of Alloyed Titanium Alloys. Modern Problems of Physical Metallurgy, Collection of Scientific Papers of Frantsevich Institute for Problems of Materials Science of N.A.S.U. 2013; p. 94. Available online: <http://dspace.nbu.gov.ua/handle/123456789/114523> (accessed on 30 March 2022). (In Russian)
30. Isabell, T.C.; Dravid, V.P. Resolution and sensitivity of electron backscattered diffraction in a cold field emission gun SEM. *Ultramicroscopy* **1997**, *67*, 59–68. [[CrossRef](#)]
31. Markovsky, P.E.; Janiszewski, J.; Stasyuk, O.O.; Bondarchuk, V.I.; Savvakina, D.G.; Cieplak, K.; Goran, D.; Soni, P.; Prikhodko, S.V. Mechanical Behavior of Titanium Based Metal Matrix Composites Reinforced with TiC or TiB Particles under Quasi-Static and High Strain-Rate Compression. *Materials* **2021**, *14*, 6837. [[CrossRef](#)]